Seasonal Cycle–El Niño Relationship: Validation of Hypotheses

HENG XIAO AND CARLOS R. MECHOSO

Department of Atmospheric and Oceanic Sciences, University of California, Los Angeles, Los Angeles, California

(Manuscript received 27 June 2008, in final form 19 November 2008)

ABSTRACT

The present paper examines ways in which the seasonal cycle influences the evolution of El Niño in the tropical Pacific. The following hypotheses and associated physical mechanisms are investigated: (i) Hypothesis 1 (H1)—the seasonal warming of the cold tongue early in the calendar year (January–April) favors the initial growth of an event; (ii) hypothesis 2 (H2)—during an event, the warm surface waters migrating in the western basin from the Southern to the Northern Hemisphere during the northern spring (April–May) trigger enhanced convection along the equator, which contributes to reinforce the event; and (iii) hypothesis 3 (H3)—the warm surface waters returning in the western basin from the Northern to the Southern Hemisphere toward the end of the calendar year (November–January) favor the demise of ongoing events.

Hypothesis-validation experiments are performed with a coupled atmosphere–ocean general circulation model (CGCM)—the tropical Pacific version of the University of California, Los Angeles (UCLA) CGCM. The anomaly-coupling technique is applied, in which the simulated seasonal cycle and interannual variability can be separated and artificially modified to highlight the aspect targeted for examination, thus allowing for comparisons of simulations in which seasonal conditions in the CGCM's atmospheric component are either fixed or time varying. The results obtained in the experiments are supportive of hypotheses H1 and H3. No supportive evidence is found for the validity of hypothesis H2.

1. Introduction

The approximate ''phase locking'' of El Niño events to the seasonal cycle (i.e., the tendency of El Niño events to peak during the second half of the calendar year) suggests that interactions between interannual and seasonal time scales are important contributors to tropical climate variability. This suggestion has motivated many studies, which have provided several hypotheses on the complex mechanisms at work for the existence of such interactions.

In the present paper we focus on the validation of three hypotheses on the seasonal cycle–El Niño relationship. The hypotheses are largely motivated by the work of Philander et al. (1984), Philander (1985), Harrison and Vecchi (1999), and Vecchi and Harrison (2003) and refer to processes in the tropical Pacific:

H1: The seasonal warming of the cold tongue early in the calendar year (January–April) favors the initial growth of El Niño events.

H2: During an El Niño event, the warm surface waters migrating in the western basin from the Southern to the Northern Hemisphere during the northern spring (April–May) trigger enhanced convection along the equator, which contributes to reinforce the event.

H3: The warm surface waters returning in the western basin from the Northern to the Southern Hemisphere toward the end of the calendar year (November–January) favor the demise of ongoing El Niño events.

Earlier work proposed that the seasonal cycle influences El Niño–Southern Oscillation (ENSO) through variations in ''coupling strength'' or ''coupling instability'' of the atmosphere–ocean system in the tropical Pacific basin (e.g., Philander et al. 1984; Philander 1985). Battisti and Hirst (1989) were the first to quantify the seasonal variations of the coupling instability. They showed that the background state in a model of the Cane–Zebiak type (Zebiak and Cane 1987) is unstable

Corresponding author address: Heng Xiao, Dept. of Atmospheric and Oceanic Sciences, University of California, Los Angeles, 7127 Math Sciences Building, 405 Hilgard Ave., Los Angeles, CA 90095–1565.
E-mail: hengx@atmos.ucla.edu

DOI: 10.1175/2008JAS2870.1

(with respect to small perturbations) during most of the seasonal cycle. The dominant influences on the seasonal variations of coupling instability were provided by those in the mean low-level convergence in the atmosphere and upwelling in the ocean. The influence of mean low-level convergence maximizes in March–April, when the intertropical convergence zone (ITCZ) is closest to the equator, and minimizes later in the year. The influence of mean upwelling maximizes in July–October and minimizes in March–April. These two influences tend to cancel each other in such a way that the combined effect is a slight maximum of the linear growth rate in July–August.

Tziperman et al. (1997, 1998) proposed an explanation for the seasonal phase locking of ENSO under the ''subsurface memory paradigm'' (Neelin et al. 1998). Their stability analysis of a linearized Cane–Zebiak model showed that the coupling instability is strongest in the northern spring and early summer and is weakest from October to the end of the calendar year. In the delayed oscillator theory—a simple and classical form of the subsurface memory paradigm—upwelling Kelvin waves generated at the western boundary by reflection of incoming Rossby waves excited 5 to 6 months before the El Niño peak in the central to eastern basin are responsible for the anomaly demise in the eastern basin. Here, the upwelling Kelvin waves compete with downwelling Kelvin waves that are excited in the central to eastern basin near the El Niño peak. In an uncoupled scenario, the upwelling waves would be weaker because the original Rossby waves are excited by relatively weak wind anomalies and energy is dissipated during reflection and propagation. In a coupled scenario, however, the situation is different. The Rossby waves are excited when the coupling instability is strongest during spring and hence can be highly amplified by positive feedbacks before reflection at the western boundary. The downwelling Kelvin waves are excited when the coupling instability is weakest around the end of the year. In this way, the upwelling Kelvin waves become dominant toward the end of the calendar year, and El Niños lock to the seasonal cycle.

Nonlinear analysis has revealed more complexities in the interactions between the seasonal cycle and ENSO. Tziperman et al. (1994, 1995) showed that changing the magnitude of prescribed seasonal variations and other parameters in the standard Cane–Zebiak model (with all the nonlinearities retained) results in different behaviors of the coupled system: (i) nonoscillatory; (ii) quasi periodic, in which the system oscillates in its own ''natural'' frequency; (iii) mode locked, in which the system is in subharmonic resonance with the seasonal forcing and oscillates with a frequency that is a rational multiple of the annual frequency; and (iv) chaotic, in which the system jumps between multiple resonances and shows strong irregularity. This variety of behaviors is consistent with the so-called quasi-periodic route to chaos for low-order nonlinear dynamic systems under external periodic forcing. Jiang et al. (1995) showed through an eigenmode analysis of a simplified Cane–Zebiak model with both constant and seasonally varying mean state that nonlinear interactions with the seasonal cycle can greatly change the temporal behavior of the oscillator. They also showed that the spatial pattern of the oscillation in the nonlinear regime with a seasonally varying background state is similar to that in the linear regime with a constant mean state. These findings give credibility to results obtained by application of normal-mode analysis to the linearized Cane–Zebiak model. They also provide an alternative explanation to ENSO's irregularity. Subharmonic resonances can also fill up the broad spectral peak in the observation.

Neelin et al. (2000) pointed out clear interevent variations in ENSO phase locking to the seasonal cycle during the last 50 yr; the variations were stronger during the onset and decaying phases of the events. They showed that models in which the source of irregularity is provided by nonlinear effects, rather than high-frequency noise, could reproduce interevent variations similar to those in the observation. Several kinds of phase-locking behavior could be obtained with the same specified mean seasonal state by simply perturbing the values of model parameters (e.g., the coupling strength). Neelin et al. (2000) concluded that the phase relationship between the interannual oscillation and the seasonal cycle is determined by complex interactions among the intrinsic oscillator, the seasonal cycle, and the random forcing by high-frequency atmospheric noise.

Although coupling instability is an essential component of our current theoretical understanding of ENSO, its dominating mechanisms at different times of the seasonal cycle are still unclear. For example, Battisti and Hirst (1989) and Tziperman et al. (1997) reached slightly different conclusions, as reviewed earlier. Tziperman et al. (1997, 1998) argued that boreal spring and early summer is most unstable to coupled anomaly growth, probably because of the warm surface conditions in the eastern basin. This is consistent with hypothesis H1 proposed earlier. Battisti and Hirst (1989) found, in a model very similar to the one used in Tziperman et al. (1997, 1998), that seasonal variation in oceanic upwelling in the equatorial region also has a large impact on coupled anomaly growth, which leads to the most unstable condition in July–August.

From April to May, the ITCZ in the Northern Hemisphere strengthens while the South Pacific Convergence Zone (SPCZ) in the Southern Hemisphere weakens.

The surface warm waters and associated atmospheric convergence zone in the western tropical Pacific migrate from the Southern to the Northern Hemisphere. Philander (1985) posited that during a growing El Niño event, the warm waters crossing the equator added to existing SST anomalies could trigger an eastward extension of convection along the equator and an increase in westerly wind anomalies in the central to eastern basin. Hence, the El Niño event would amplify H2.

Other paradigms have been suggested for the El Niño–seasonal cycle relationship by studies performed in contexts less specialized than the delayed oscillator. Harrison and Vecchi (1999) and Vecchi and Harrison (2003) proposed that the shift of the westerly wind anomalies around the date line from on the equator to south of it at the end of the calendar year is responsible for halting El Niño growth in the eastern basin. The shift is linked to the seasonal southward migration of the oceanic surface warm waters (and associated convective activity) around November and December. The wind anomaly shift generates upwelling Kelvin waves, which eventually cancel the warm sea surface temperature (SST) anomaly in the eastern basin. Studies with atmospheric and oceanic general circulation models (AGCMs and OGCMs, respectively) (Vecchi and Harrison 2006; Vecchi 2006; Spencer 2004) have produced supportive evidence for this hypothesis, which is consistent with H3. Wang et al. (1999) and An and Wang (2001) also argued that the atmospheric condition in the western basin toward the end of the year is suitable for the development of equatorial easterly wind anomalies, which favor El Niño demise, even though their explanation of the phase transition is quite different from that of Harrison and Vecchi (1999). Other studies argued that oceanic processes like the advection of heat content anomalies by the seasonally varying mean circulation (e.g., Guilyardi et al. 2003; Vintzileos et al. 1999) or the impact of the seasonal variation in the equatorial thermocline structure (e.g., An and Wang 2001; Galanti et al. 2002) may also be important. Recently, Chang et al. (2007) suggested that the seasonality of the high-frequency variability related to the Pacific meridional mode could lead to seasonal phase locking of El Niños.

The present work carries out a quantitative validation of hypotheses H1–H3. A major obstacle for this task has been the lack of realistic coupled setups, in which most if not all potential participating mechanisms are present, together with the lack of testing methods that can separate different mechanisms. Overcoming this obstacle to the largest possible extent determines our methodology for research. In setting the control environment for the performance of hypothesis-validation studies, we choose to concentrate on a simulation by the University of California, Los Angeles (UCLA) coupled atmosphere–ocean GCM (CGCM); this strategy has merits and demerits. The most important merit is that the seasonal cycle and interannual variability can be easily identified and altered in view of the aspect selected for examination. The most important, and obvious, demerit is that the seasonal cycle and departures from it in CGCM simulations are not perfect portrayals of reality. It will be argued, however, that the unrealistic features are not likely to challenge our results.

The plan of the paper is as follows: Section 2 introduces the CGCM used in this study and describes selected aspects of its performance; it also describes how the anomaly-coupling technique was implemented to achieve our objectives. Section 3 presents the results of the experiments conducted with the CGCM. Section 4 gives a summary of our results. In section 5 we discuss our findings and outline future work.

2. The CGCM and the anomaly-coupling method

a. The CGCM

This work is based on the CGCM used in Yu and Mechoso (2000) and Mechoso et al. (2003). This particular model consists of the UCLA AGCM version 6.8 (Suarez et al. 1983; Mechoso et al. 2000, and references therein) and the OGCM known as the Geophysical Fluid Dynamics Laboratory (GFDL) Modular Ocean Model (MOM) version 1.1 (Bryan 1969; Cox 1984; Pacanowski et al. 1991). The AGCM includes the schemes of Deardorff (1972) for the calculation of surface wind stress and surface fluxes of sensible and latent heat, Katayama (1972) for shortwave radiation, Harshvardhan et al. (1987) for longwave radiation, Arakawa and Schubert (1974) for parameterization of cumulus convection, and Kim and Arakawa (1995) for parameterization of gravity wave drag. This version incorporates the revised formulation of PBL and stratocumulus processes of Li et al. (1999), which improves the simulation of marine stratocumulus. The AGCM has 15 layers in the vertical (top at 1 mb) and a horizontal grid spacing of 4° latitude × 5° longitude. The MOM includes the scheme of Mellor and Yamada (1982) for parameterization of subgrid-scale vertical mixing by turbulence processes. The surface wind stress and heat flux are calculated hourly by the AGCM, and the daily averages are passed to the OGCM. The SST is calculated by the OGCM, and its value at the time of coupling is passed to the AGCM. The ocean model domain covers the tropical Pacific from 30°S to 50°N and from 130°E to 70°W. The OGCM has 27 layers in the vertical with 10-m resolution in the upper 100 m. The

ocean has constant depth of about 4150 m. The longitudinal grid spacing is 1°; the latitudinal spacing varies gradually from 1/3° between 10°S and 10°N to almost 3° at 50°N. The time-varying climatology from Alexander and Mobley (1976) is used to prescribe the SSTs outside the OGCM domain. ''Sponge layers'' are set up at the northern and southern boundaries of the ocean domain to reduce the errors related to the artificial zonal boundaries in the open ocean. In these layers, both 10° wide in latitude, temperature and salinity are relaxed toward observed climatology. No ad hoc corrections are applied to the fields exchanged by model components. The CGCM is spun up and run for 53 yr. Our analysis focuses on the last 43 yr of the run. We will refer to this run as Control.

The selected CGCM version is not the most up-to-date among those we apply in our own climate studies, but it has two important advantages. First, as will be demonstrated in the next subsection, the model is reasonably successful in the simulation of the mean state, seasonal cycle, and interannual variations in the tropical Pacific basin with relatively modest computer requirements. Second, because the model was used in several previous studies, we are able to profit from experiences gained in runs and analyses completed in the past.

b. Selected results obtained in Control

1) MEAN CLIMATE AND SEASONAL CYCLE

For the simulated mean climate and seasonal cycle in the tropical Pacific, we concentrate on the features highlighted in section 1. The reader is referred to Xiao (2008) for a more complete description of the model's performance.

Figures 1a and 1b show the distribution of annual mean SST in the simulation and the observation. The simulation captures pattern and values reasonably well. There is, however, an overall warm bias that ranges from 0.5° to 1°C. The simulated pattern appears too zonal, and the warm pool in the west and the equatorial cold tongue in the east are both too narrow in latitude. South of the equator, the warm water from the western basin extends beyond 100°W, which is too far east. Figures 1c and 1d display the annual mean precipitation in the simulation and the observation. Again, there is a reasonable pattern agreement, except that the simulated SPCZ extends too far east along the equator. This feature is usually referred to as the double-ITCZ bias; it is a common problem for most state-of-the-art CGCMs (e.g., Mechoso et al. 1995; de Szoeke and Xie 2008). In addition, the simulated ITCZ in the Northern Hemisphere has a sharper maximum in the western basin and is weaker in the eastern basin.

For H1 we are interested in the seasonal warming of the cold tongue and related increase in rainfall early in the year. Figure 2 displays features of the seasonal change in monthly mean SST and precipitation from January to April in the simulation and the observation. According to Fig. 2a, the observation shows in the eastern basin a surface warming of 1°–2°C, an increase in rainfall between the equator and 10°S of about 3 mm day^{-1}, and an enhancement in the ITCZ rainfall just north of the equator. The simulation (Fig. 2b) captures the surface warming, but this is more confined to the equatorial band (5°S–5°N). The simulation also captures the increase of rainfall in the tropical southeastern Pacific, albeit with slightly smaller magnitude. The ITCZ rainfall in the eastern basin tends to be weak, and the strengthening of this feature just north of the equator in the period under consideration is missed.

For H2 and H3, we are interested in the meridional migration with season of the surface warm waters and the overlying atmospheric convergence zones in the western basin. According to Fig. 3a, in the western basin during boreal winter and spring the observation shows strongest SPCZ rainfall and warmest SSTs south of the equator. Later in the year, the SPCZ weakens and the ITCZ north of the equator strengthens to maximize in July and August. The warm waters in the western basin also move northward at this time of the year. Figure 3b shows that the simulation reproduces the timing of this seasonal movement of surface warm waters and overlying convergence zones reasonably well, although the magnitude of those features is slightly overestimated.

2) INTERANNUAL VARIABILITY

The interannual variability in Control is summarized in the panels of Fig. 4. Figure 4a shows the Niño-3 SST anomaly (SSTA) index, defined as the monthly mean SST anomaly averaged in the eastern equatorial basin (5°S–5°N, 150°–90°W). In this study we label as El Niño (La Niña) events in the simulation those periods in which the Niño-3 index is warmer than 0.5°C (colder than −0.5°C) for more than three consecutive months. [Neelin et al. (2000) used the same definition in their inspection of observational data.] In the 43-yr run that we are analyzing, our definition yields eight warm events and nine cold events; these are marked by the circles on the figure. To examine the relationship between the phase of El Niño and the seasonal cycle, Fig. 4b shows the variance of the Niño-3 SSTA index binned into each calendar month for the simulation and the observation. The observation shows minimum variability between March and April, which marks the time of event initiation from very small anomalies, and maximum variability around November and December, which marks

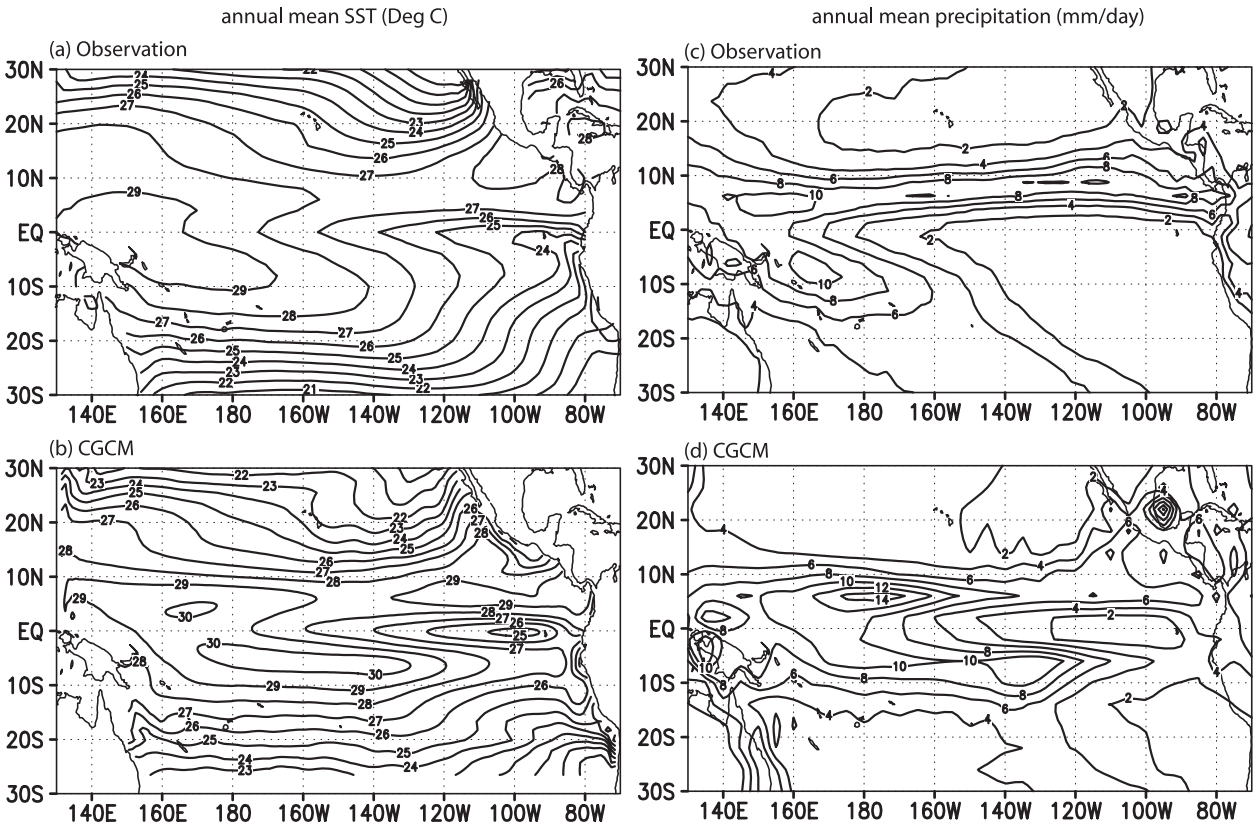

FIG. 1. Annual mean SST (°C) in the tropical Pacific from (a) the 1971–2000 climatology from the National Climatic Data Center (NCDC) extended reconstructed SST (ERSST) dataset version 3 (Smith et al. 2008) and (b) the control simulation. Annual mean precipitation (mm day^{-1}) from (c) the Climate Prediction Center Merged Analysis of Precipitation (CMAP) data provided by the NOAA/OAR/ESRL PSD (available online at http://www.cdc.noaa.gov) (Xie and Arkin 1997) and (d) the control simulation.

the time of peak anomalies during ENSO events. The simulation captures the timing of the minimum, but the maximum variability is in July and August.

Figure 4c shows the global average wavelet spectra of the Niño-3 total SST index for both the simulation and the observation, as produced by the software package of Torrence and Compo (1998). Here the global average wavelet spectrum is just the wavelet spectrum averaged over the temporal domain. The simulation produces a significant interannual peak with amplitude comparable to that of the seasonal peak, in agreement with the observation. The amplitudes of both seasonal and interannual variations in the simulation, however, are smaller (about half) than in the observation. Also, the observation shows a broad spectral peak between 2 and 7 yr, with a split around 4 yr and local maxima around 3.5 and 5 yr. In the simulation, the main peak is at around 5 yr and there is a weaker peak that appears at around 3 yr. The simulation obtains a significant peak around 11–12 yr, without a counterpart in the observation.

Table 1 compares statistics of SSTA indices defined for different regions in the equatorial band in the simulation (all 53 yr) and the observation (1950–2000). Skewness and kurtosis measure the extent to which a probability distribution deviates from the normal one. The large values of those parameters in the distribution of SSTA corresponding to the eastern equatorial Pacific and along the South American coast (as represented by the Niño-3 and Niño-12 indices) indicate that the ENSO oscillation is most nonlinear in this region (Burgers and Stephenson 1999). The standard deviation of SSTA indices is smaller in the simulation, indicating weaker ENSO amplitudes. The skewness and kurtosis are also smaller, suggesting that the nonlinearity of ENSO is weaker in the simulation than in the observation.

3) ATMOSPHERIC HIGH-FREQUENCY VARIABILITY

It has been argued that high-frequency atmospheric variability related to the Madden–Julian oscillation (MJO) and tropical weather—namely, westerly wind burst (WWB) events—has important impacts on the development of ENSO events and may have important energy exchanges with the interannual oscillation (e.g., Vecchi

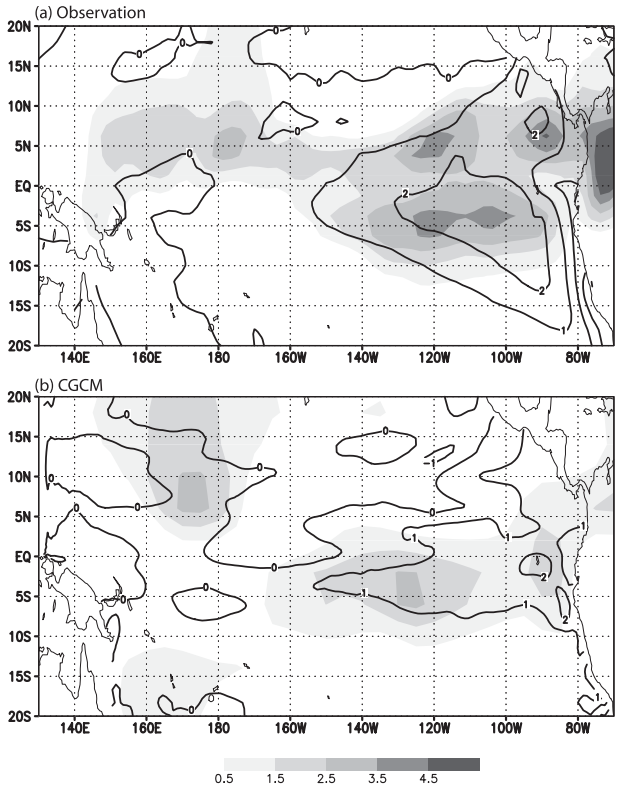

FIG. 2. Seasonal changes from January to April (April minus January) in monthly mean SST (°C; contours) and precipitation (mm day^{-1}; shading) for the tropical Pacific from (a) the observations (SST from the NCDC ERSST dataset; precipitation from CMAP) and (b) the control simulation.

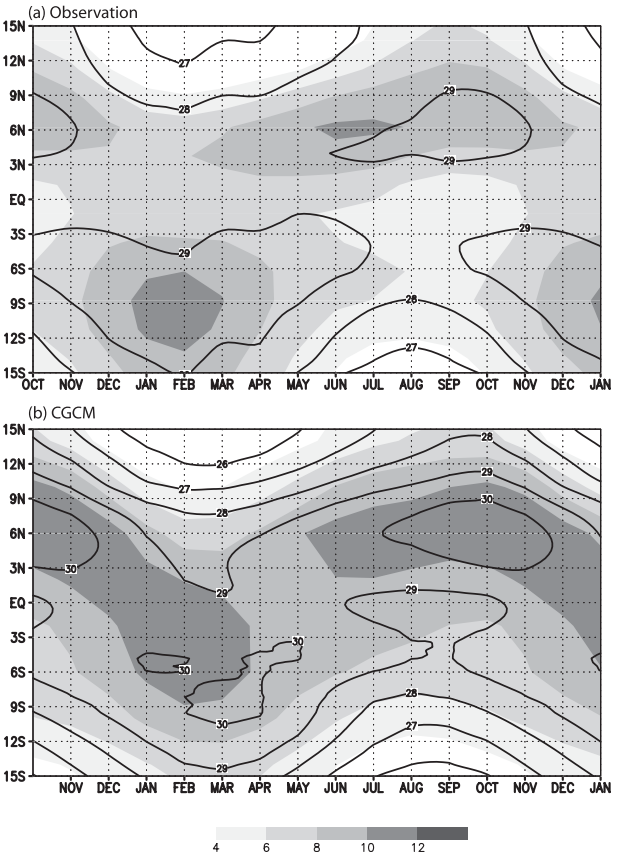

FIG. 3. Seasonal migration of warm surface waters indicated by SST (°C; contours) and of convergence zones, indicated by precipitation (mm day^{-1}; shading), in the western basin (averaged between 150°E and 170°W) from (a) the observation (SST from the NCDC ERSST dataset; precipitation from CMAP), and (b) the control simulation.

and Harrison 2000; McPhaden et al. 1992; McPhaden 1999; Kessler 2002). Several authors have examined the intraseasonal variability associated with MJO and its impact on the ''bulk'' interannual oscillation (e.g., Moore and Kleeman 1999; Kessler and Kleeman 2000). In the CGCM we are using, the variability of surface wind in the 30–60-day frequency band is much weaker than in the observations over the tropics [see Xiao (2008) for more details]. This lack of MJO activity, however, does not affect the existence of interannual variability in the model.

WWB events due to submonthly atmospheric variations (6–30 days) can also influence ENSO characteristics (e.g., Vecchi and Harrison 2000). It has been argued, however, that WWBs associated with frequencies higher than 20–30 days play a much less important role than the lower-frequency component of the MJO (30–60 days) in affecting ENSO (e.g., Roulston and Neelin 2000; McPhaden et al. 2006). Figure 5a shows in Hovmöller format the monthly mean variance of daily surface zonal wind averaged in the equatorial band (5°S–5°N) as an indicator of submonthly variability. In general, the region west of 160°W contributes most of the variance, with amplitudes on the order of 6–10 m^2 s^{-2}. During El Niño (La Niña) events, as indicated in Fig. 5c by the Niño-3 SSTA index, the band of large variance expands to the east of 160°W (retreats to the west of 160°W). In strong El Niño events, like the one in year 28, this band expands east of about 120°W. To further examine the temporal modulation of the high-frequency variability in the western to central basin (150°E–130°W), we divide the region into two parts east and west of 170°W. The black and gray lines in Fig. 5b show monthly variance of daily surface zonal wind averaged in the region west and east of 170°W, respectively. The black line shows a clear seasonal modulation, with a peak in high-frequency variability in boreal winter (December–February). There are also low-frequency modulations with a frequency that is decadal rather than interannual. The gray line clearly marks the eastward extension of high-frequency variability during large

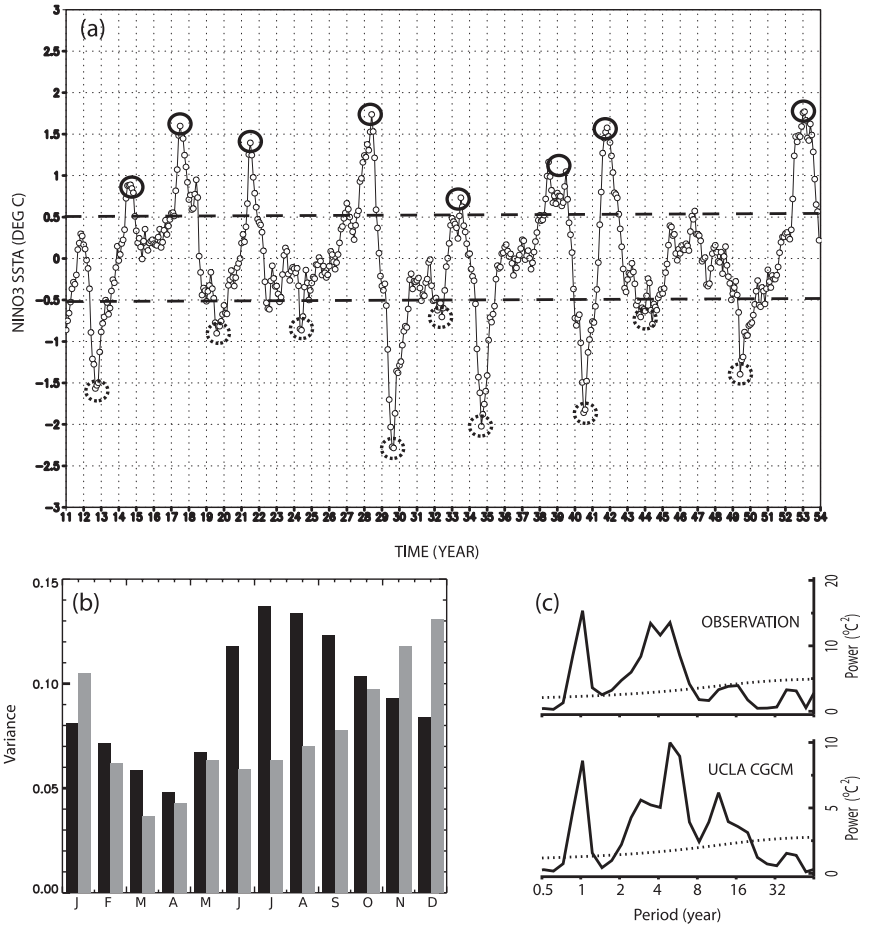

FIG. 4. (a) Monthly Niño-3 SSTA index (°C) from years 11 to 53 of the control simulation. (b) Variance of the monthly Niño-3 SSTA index binned into each calendar month for the observations (NCDC ERSST dataset; gray bars) and the control simulation (black bars). (c) Power spectra of the Niño-3 total SST index for both (top) the NCDC ERSST dataset and (bottom) the control simulation. The dotted lines in (c) indicate the 95% confidence level. The spectra in (c) are global wavelet spectra produced with the wavelet package from Torrence and Compo (1998).

El Niño events. The exact relationship between the submonthly variability and ENSO in our simulation is unclear at this point. The analysis above does suggest that in this MJO-less scenario the spatial and temporal modulation of high-frequency variability is still linked to the seasonal and interannual variations. Whether this linkage is interactive in the CGCM simulation as well as in the observation begs further clarification (e.g., Eisenman et al. 2005).

c. The anomaly-coupling method

The atmospheric and oceanic components of the CGCM exchange information at time intervals set at the beginning of the run. The atmospheric component provides cumulative means between coupling instances of surface heat, momentum, and freshwater fluxes; the oceanic component of the CGCM provides the SST. The coupling interval in the model version used in this study is 24 h. The anomaly-coupling technique was originally developed in an attempt to minimize the contribution to the CGCM climatological drift by either predicted or simulated errors. The idea is to steer the interface climatology of each model component to approximately follow its counterpart in the observation. The first step in the procedure consists of splitting the field to be passed by each model into two parts: (i) the part corresponding to the climatology as obtained in an uncoupled run with forcing from the observation and (ii) the remainder, which is defined as the anomaly. Next, the field to be passed is determined by adding this anomaly to the observed climatology. In short, the climatological parts of the fields exchanged between model components are replaced by those in the observation while leaving the anomalous parts without modification.

TABLE 1. Standard deviation, skewness, and kurtosis for several equatorial SSTA indices from the control simulation (53 yr) and *World Ocean Atlas 2005* (Locarnini et al. 2006) SST observations (1950–99) separated by a slash (Control/CGCM).

	Niño-4 (5°S–5°N, 160°E–150°W)	Niño-3.4 (5°S–5°N, 120°–170°W)	Niño-3 (5°S–5°N, 90°–150°W)	Niño-12 (10°S–0°, 80°–90°W)
Std dev	0.61/0.43	0.87/0.69	0.92/0.69	1.16/0.57
Skewness	−0.29/−0.79	0.31/−0.21	0.79/−0.08	1.21/−0.07
Kurtosis	−0.36/0.42	0.14/−0.17	1.15/0.41	2.17/0.55

Kirtman et al. (1997) provide details on the numerical procedure and verification of the method.

Because our primary interest is the relationship between the seasonal cycle and El Niño, we implement the anomaly-coupling technique to eliminate the seasonal cycle in the AGCM and to prescribe the seasonal cycle in the OGCM to that in Control (see the schematic in Fig. 6). The details of the implementation procedure are as follows. In the AGCM, all time-varying external conditions, except for SST (i.e., surface roughness, albedo, solar declination, etc.), are set to those at the start time; the SST is the OGCM-provided field to which climatology from Control at the time of coupling was subtracted, and that corresponding to the start time was

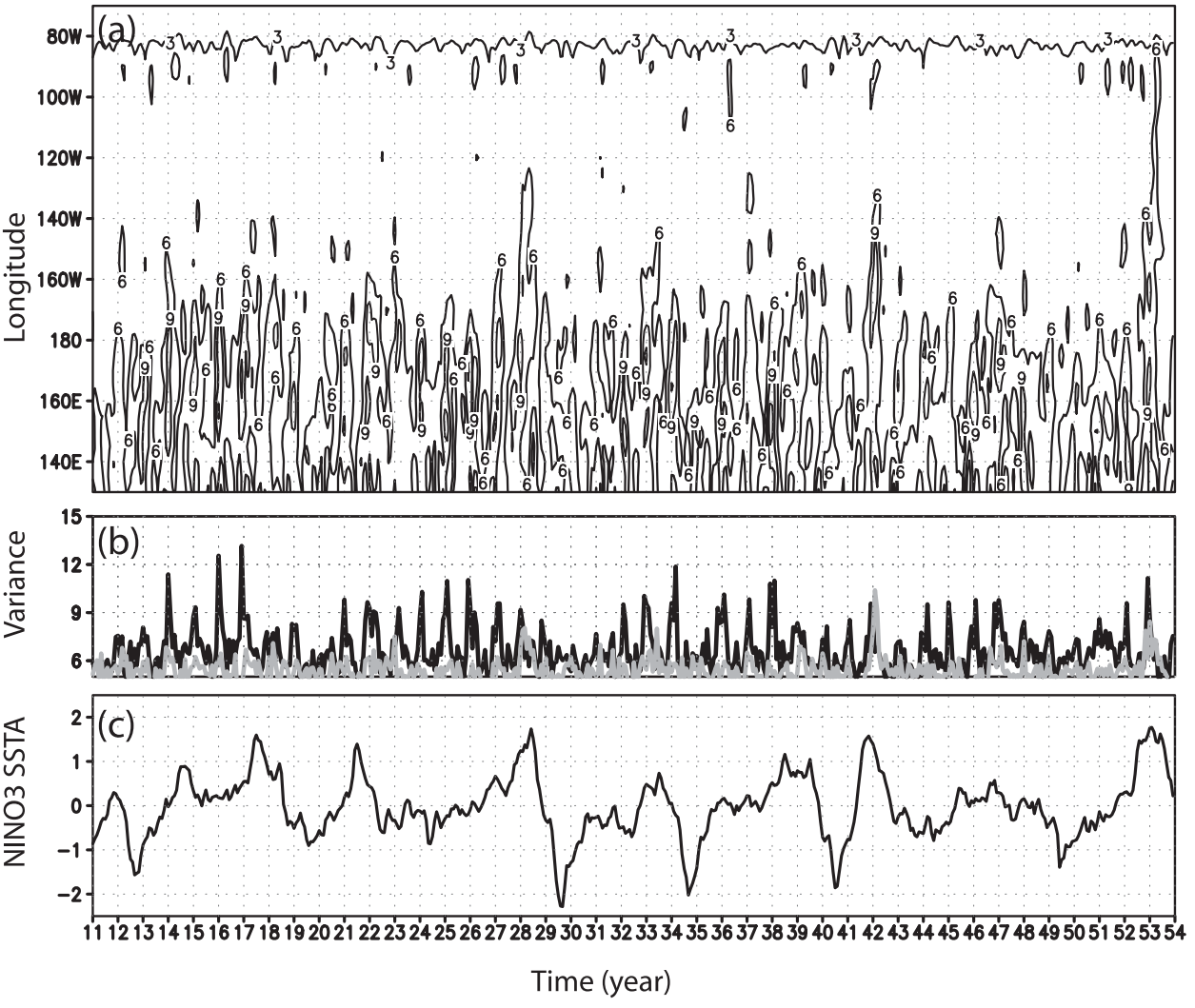

FIG. 5. (a) Monthly variance of daily surface zonal wind (contour interval 3 $m^2\ s^{-2}$) averaged in the equatorial band (5°S–5°N) from years 11 to 53 of the control simulation. (b) Area average of monthly variance of daily surface zonal wind for the western basin (5°S–5°N, 150°E–170°W, black line) and central basin (5°S–5°N, 170°–130°W, gray line). (c) Niño-3 SSTA index from the same period.

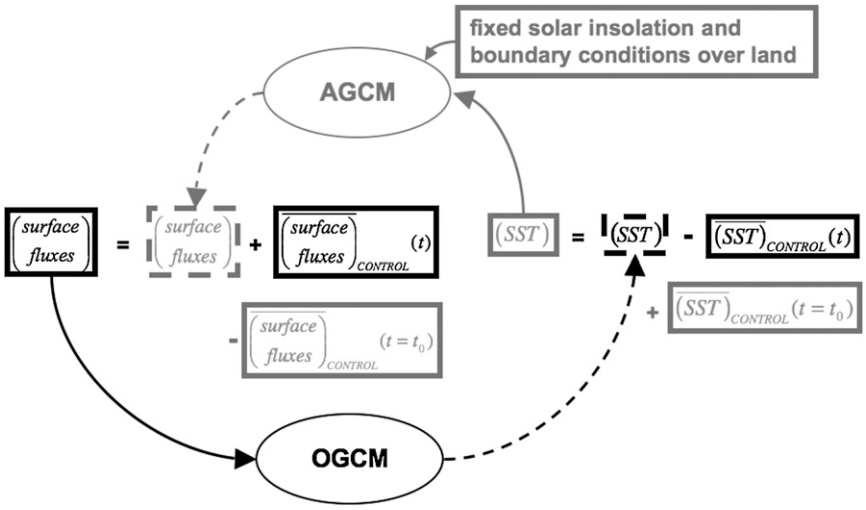

FIG. 6. Schematic illustration of the anomaly-coupling strategy used in our experiments. The coupling information is modified as it passes through the model's coupling subroutines. The mean seasonal SST (black box) passed to the AGCM is replaced with a fixed field corresponding to the restart date (gray box), while the surface fluxes passed from the seasonless AGCM to the OGCM is modified by subtracting the corresponding mean fluxes (gray box) and adding back the normal mean seasonal fluxes (black box). At the same time, all time-varying external conditions for the AGCM except SST are fixed consistently.

added. In the OGCM, the surface fluxes are the AGCM-produced fields to which the climatology from Control at the start time was subtracted, and that corresponding to the time of coupling was added. The CGCM run with such anomaly coupling is then compared with that from Control with normal coupling. All initial conditions are taken from Control.

A priori anomalies obtained with our anomaly-coupling procedure can have a nonzero projection onto the mean climatology. We have verified a posteriori that this projection is negligible in our runs. In addition, we did not encounter any technical difficulties using the technique, and ''initial shocks'' and systematic ''climate drifts'' produced in the coupled system were also negligible.

3. Experiments and main results

This section describes the results of the experiments performed with the CGCM to validate hypotheses H1, H2, and H3 (described in the introduction). The experiments performed are listed in Table 2. Each experiment consists of one pair of nine-member ensembles of year-long runs, one with normal coupling and the other with anomaly coupling. In the AGCM, the initial conditions of the ensemble members correspond to nine consecutive days in Control, centered on the one identified as the experiment start date; in the OGCM, the initial conditions are identical in all ensemble members and correspond to the experiment start date in Control.

As stated in section 2b(2), simulated ENSO events tend to start at approximately the right time, but they peak too early in the calendar year. Therefore, the choice of control event for H1 and H2 is straightforward and we have selected the El Niño event in Year 17. The choice of control event for H3 requires more care. Nevertheless, there are strong interevent variations among simulated ENSO events and some mimic the observations more closely than others. This is the case for El Niño in Year 41, which peaks close to the year's end. Hence, we select this case as control for testing H3. We show in Fig. 7 the evolution of simulated SST in the selected events, which we will refer to hereafter as E17 and E41. Note that we will also test H2 with E41.

a. *Experiment A: From 1 January, year 17 of Control (case E17)*

Experiment A addresses hypothesis H1—that is, the effects on El Niño events of increased convective

TABLE 2. The experiments performed and the hypothesis addressed in each of them (see section 1). The restart times of the experiments are marked by the dotted lines in Fig. 7.

Experiment start date	Hypotheses to be investigated
A: 1 January, year 17	H1
B: 1 April, year 17	H2
C: 1 April, year 41	H2
D: 1 October, year 41	H3

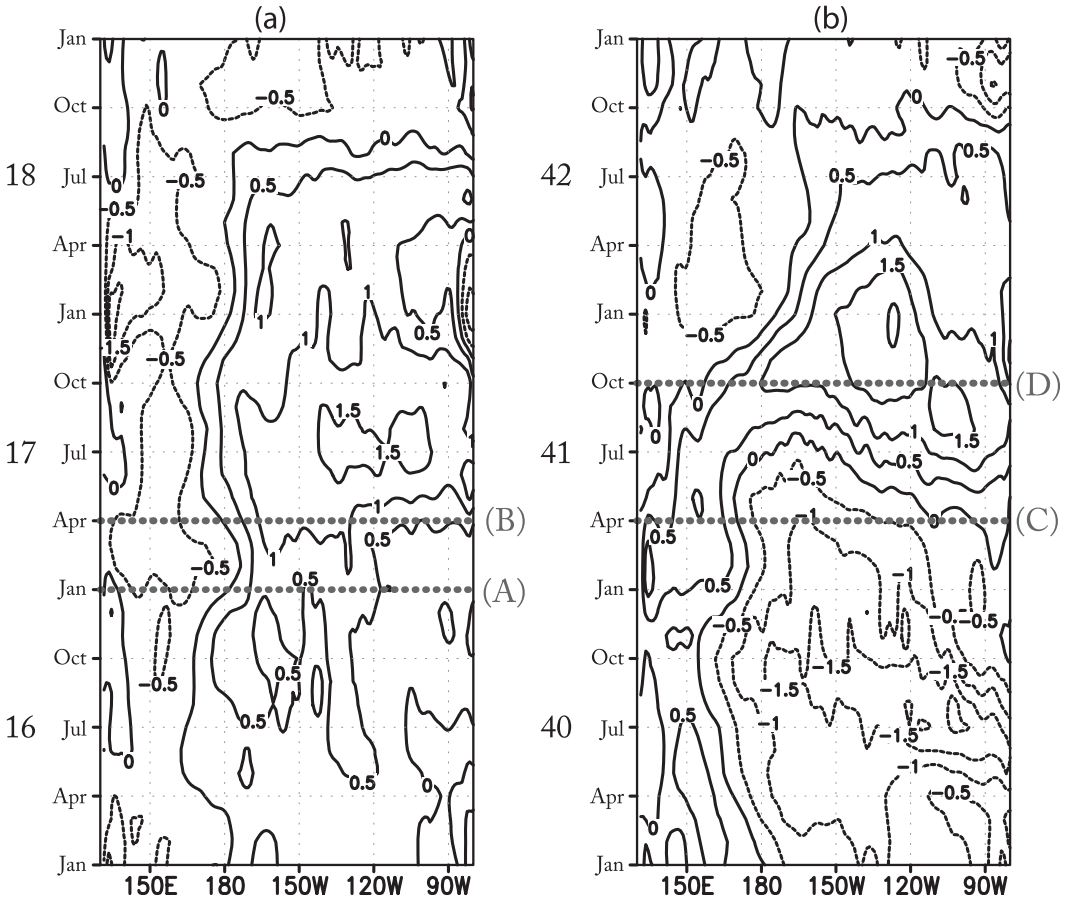

FIG. 7. Monthly SST anomalies at the equator in the control simulation (a) from January, year 16 to January, year 19, and (b) from January, year 40 to January, year 43. The dotted lines indicate the restart times of the four experiments listed in Table 2.

activity and precipitation associated with the seasonal warming of the tropical eastern basin that starts around January and peaks around April. Figure 8a shows the evolution of the Niño-3 SSTA indices for all runs in this experiment. Results in the anomaly-coupling and normal-coupling ensembles are plotted in blue and red, respectively.

The differences between ensembles are substantial by April and become stronger than 0.5°C by June. (Recall that peak values in the selected event appear in July and are about 1°–2°C). In February (i.e., 1 month after the start of the experiment) there are clear differences in the wind stress around the date line (Figs. 9a,b): the strong patch of westerly anomalies from 8°S to 8°N in the normal-coupling ensemble practically disappears in the anomaly-coupling ensemble except for some weak anomalies south of the equator. The differences in SST anomalies around the date line, however, are very small (Figs. 9c,d).

To gain insight into the processes that contribute to the differences between wind stress anomalies around the date line, we also plot in Fig. 9d the mean SST change from January to February in the Control climatology (i.e., the difference between the monthly mean SST distributions seen by the AGCM in the two ensembles), together with the February mean SST anomaly from the normal-coupling ensemble. As we can see, climatological SSTs increase from January to February by more than 0.5°C along the equator from the eastern Pacific up to about 160°W. The precipitation change from January to February is also positive in the central to eastern equatorial basin (cf. Fig. 2), which indicates that background convective activity increases. Thus, for very similar SST anomalies in both ensembles, the stronger wind anomalies in the normal-coupling ensemble must be associated with the seasonal increase in background convective activity.

In reference to the ocean, Figs. 9e and 9f show vertical cross sections along the equator of ensemble mean ocean temperature anomalies in February. The differences are larger at the subsurface (on the order of 1°C),

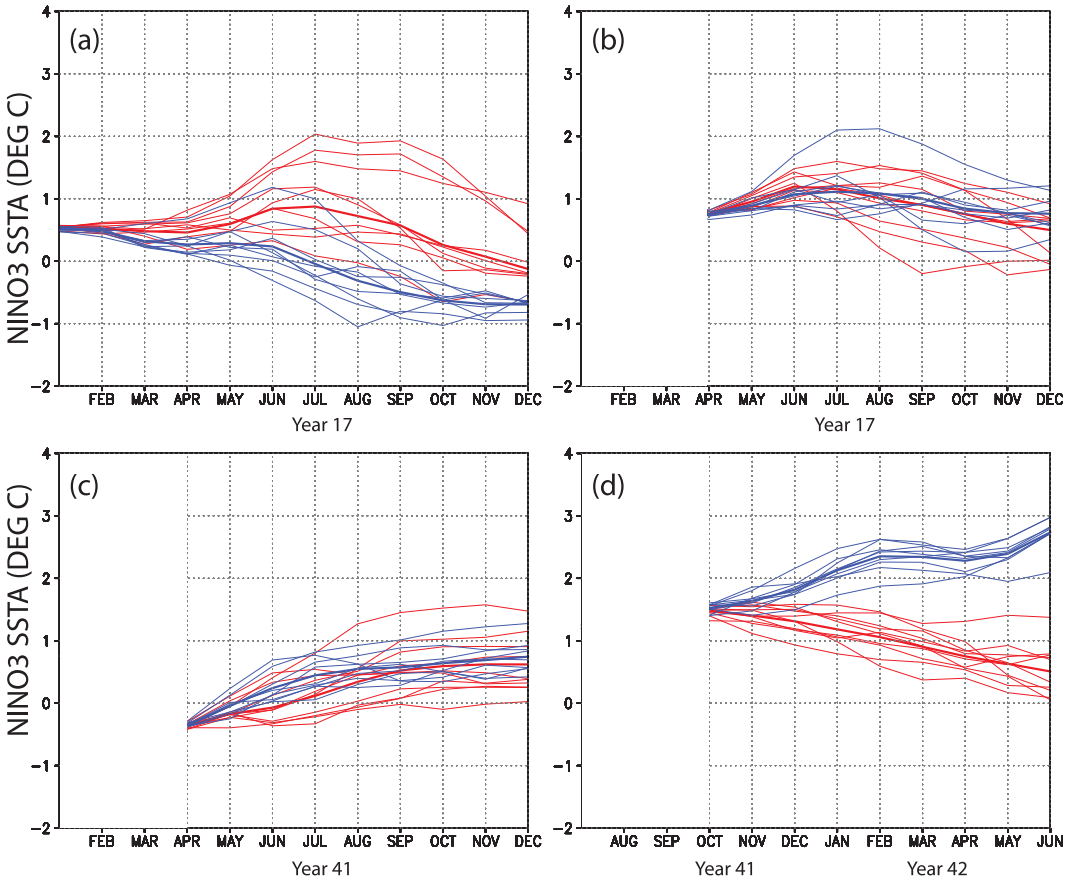

FIG. 8. Monthly mean Niño-3 SSTA indices for the normal-coupling ensemble (red thin lines) and the anomaly-coupling ensemble (blue thin lines) from experiments (a) A, (b) B, (c) C, and (d) D. Ensemble means are indicated by the thick lines.

which indicates that wind stress anomalies around the date line affect the eastern basin mainly through propagation of subsurface anomalies.

Figure 10 displays the time evolution of wind stress anomalies around the date line. From January to April, the strongest westerly anomalies in both the anomaly-coupling and normal-coupling ensembles are south of the equator, at locations coincident with those of maximum background convection. In the normal-coupling ensemble, the seasonal warming is associated with westerly anomalies extending along the equator; in the anomaly-coupling ensemble, the warming is absent and easterly wind anomalies extend along the equator. The equatorial westerly wind anomalies in the normal-coupling ensemble are consistent with the excitation of downwelling (warming) Kelvin waves, which contribute to the coupled growth of anomalies in the central to eastern basin. The peak difference in equatorial winds is around March; afterward the meridional structure of the wind stress anomalies in the normal-coupling ensemble undergoes a structural change. (We examine this change further in section 3b.) By April, the presence of cold subsurface temperature anomalies in the eastern basin (see Fig. 11) strongly indicates that the event growth is very unlikely to continue in the anomaly-coupling ensemble.

We find, therefore, that increased background convective activity in the central to eastern Pacific along the equator, associated with the seasonal warming of the equatorial cold tongue at the beginning of the year, encourages the coupled growth around the equator of anomalous westerly wind patches in the central basin and of SST anomalies to the east. The growth is helped by the eastward propagation and surfacing of subsurface temperature anomalies that originated in the west. In reality, this mechanism should be more efficient during the initial growth of a warm event, when the atmospheric convection in the central basin is still sensitive to increases in the underlying SST (see Graham and Barnett 1987). Thus, the results of experiment A validate H1.

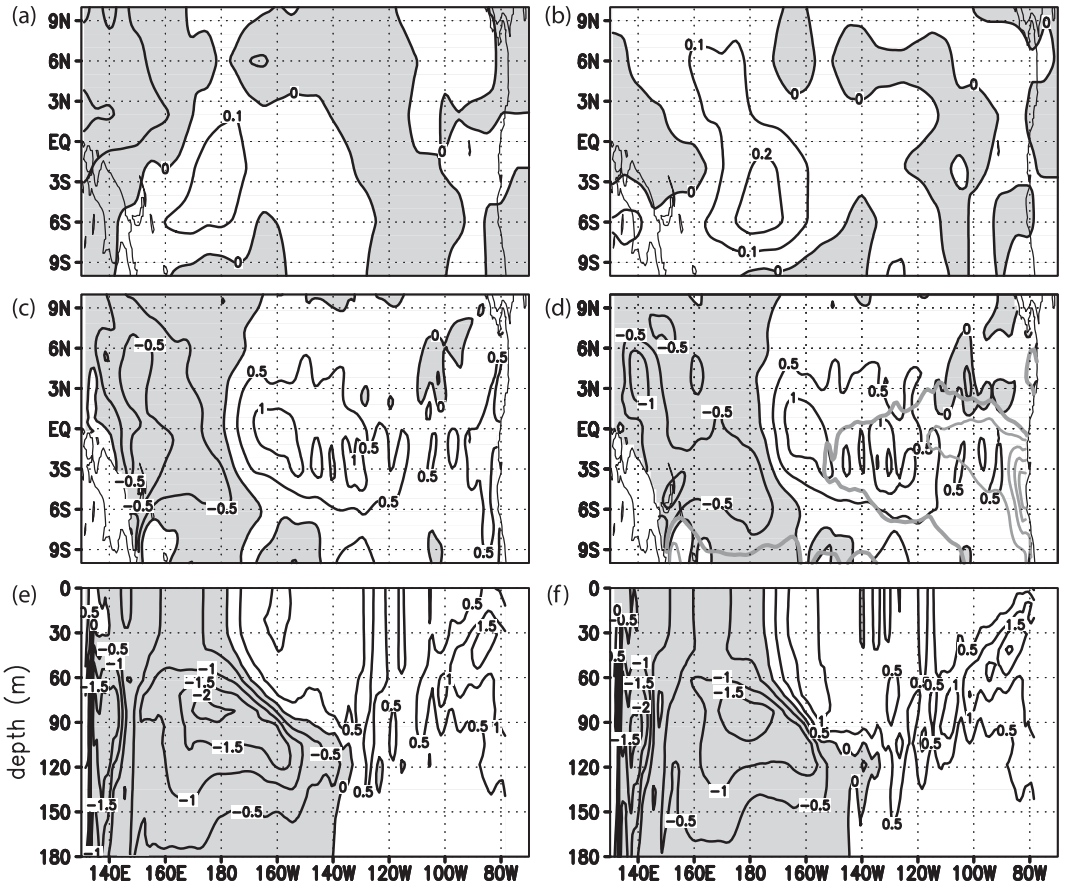

FIG. 9. Monthly mean anomalies from experiment A in February of year 17 of (a),(b) surface zonal wind stress (dyn cm^{-2}), (c),(d) SST (°C), and (e),(f) the vertical temperature (°C) cross section at the equator for (left) the anomaly-coupling and (right) the normal-coupling ensemble. In (d), the gray contours (0.5°C interval; the 0.5°C contour is thickened) show the climatological SST difference at this time between the anomaly-coupling (January) and normal-coupling ensembles (February).

b. Experiment B: Ensembles from 1 April, year 17 of Control (case E17)

If 1 April is selected as the initial condition, warm SSTs and convergence zones in the western basin do not migrate northward in the anomaly-coupling ensemble. Also, in the eastern basin, the ITCZ remains close to the equator and SSTs remain warm on the south of the equator. Thus, experiment B addresses the relative importance of the convergence zone migration in the atmosphere in the western basin in reference to the seasonal warming of the ocean in the eastern basin.

Figure 8b shows the evolution of the Niño-3 SSTA indices for all runs in experiment B. The results in the ensembles are almost identical to each other, with the differences between the averages being less than 0.2°C. Figure 12 shows the ensemble mean anomaly fields for June (i.e., 2 months after the start of the experiment). In the normal-coupling ensemble (see Fig. 12b), westerly wind stress anomalies are maximal just west of the date line north of the equator and dominate along on the equator to about 110°W. Philander (1985) refers to this feature as an eastward ''extension'' of convective activity. In the anomaly-coupling ensemble (see Fig. 12a) there are two westerly maxima—both south of the equator—one of which is west of the date line, while the other is around 120°W. The warmer mean SSTs in the eastern basin seem to contribute to the second maximum, which does not have a counterpart in Fig. 12b. By July (see Fig. 13), the SST anomaly pattern in the normal-coupling ensemble is centered on the equator, and that in the anomaly-coupling ensemble is centered south of the equator and tends to have a smaller zonal extent. Returning to Fig. 8b, it is apparent that on average SST anomalies in the equatorial Pacific are very similar in both ensembles, despite the quantitative differences displayed in Fig. 13.

Our interpretation of these results is that the positive impact on El Niño growth of the northward seasonal

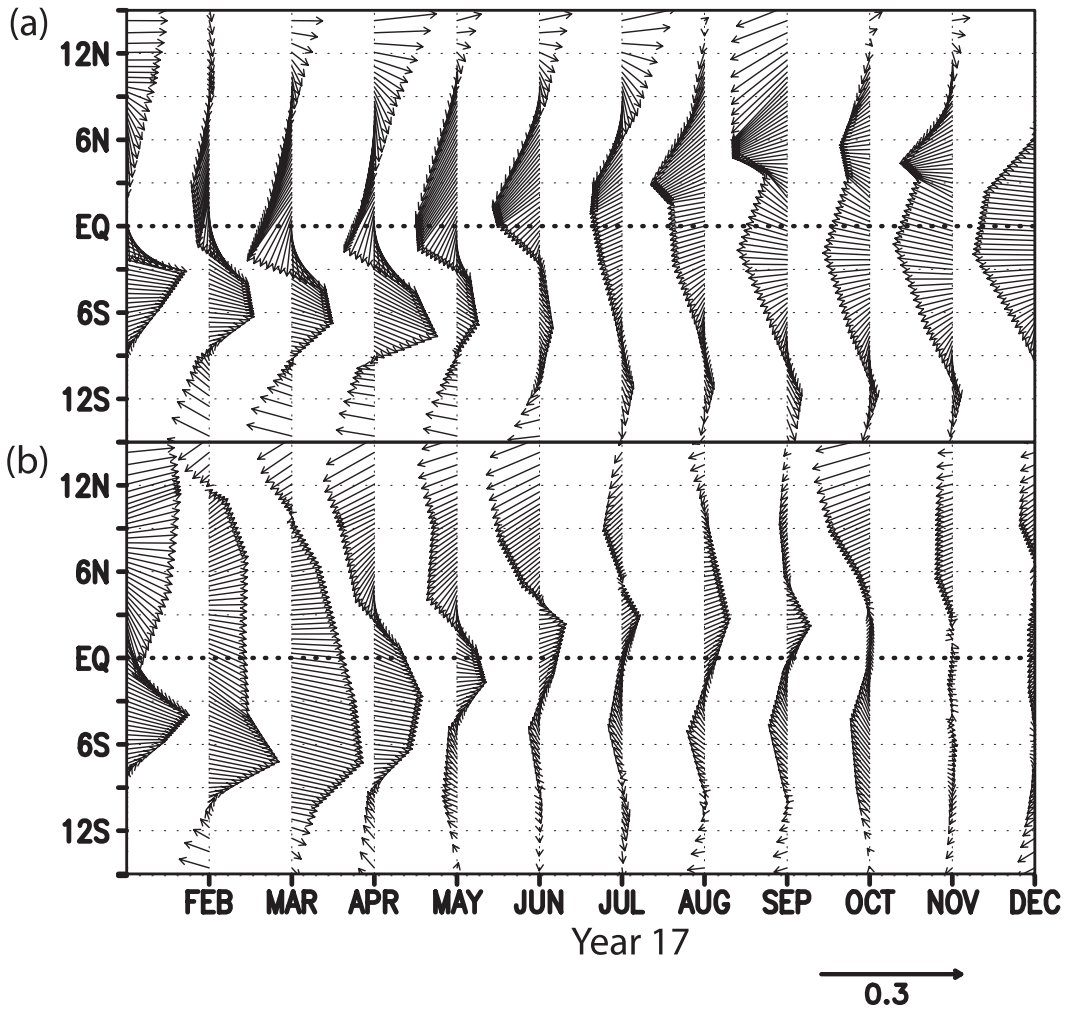

FIG. 10. Evolution of monthly mean surface wind stress anomaly (dyn cm^{-2}; January–December, year 17) in experiment A averaged in the western to central basin (150°E–170°W) for the (a) anomaly-coupling and (b) normal-coupling ensemble means.

migration of the convergence zone in the western basin and eastward extension of convection along the equator, if they exist, is cancelled by the negative impact of the restrengthening of the cold tongue after April and the associated reduction in convective activity. Thus, the results of experiment B do not validate H2.

c. *Experiment C: Ensembles from 1 April, year 41 of Control (case E41)*

Experiment C starts from the same date as experiment B, but in the year of a warm event with a different evolution (E41); hence, the two experiments target the same seasonal feature. In April, the warm event in year 41 (E41) shows only weak anomalies along the South American coast, whereas the event in year 17 (E17) starts developing early in the year and includes SST anomalies warmer than 2°C in the central basin. One can reasonably assume that these weak coastal anomalies would be even more insensitive to the changes in convection in the western basin at this time of the year than the large equatorial SST anomalies in E17, whereas the seasonal cooling in the eastern basin would have a larger impact.

Figure 8c shows the evolution of the Niño-3 SSTA indices for all runs in experiment C. Anomalies grow faster in the anomaly-coupling ensemble during April to July than in the normal-coupling ensemble. By July, the average difference between the two ensembles is about 0.5°C. The ensemble mean anomaly fields of SST and zonal wind stress for July are shown in Fig. 14. The patch of westerly wind and SST anomalies in the eastern basin (centered around 120°W) in the anomaly-coupling ensemble indicates that local coupling and amplification, rather than features in the western basin, cause the difference displayed in Fig. 8c. Thus, in experiment C we find

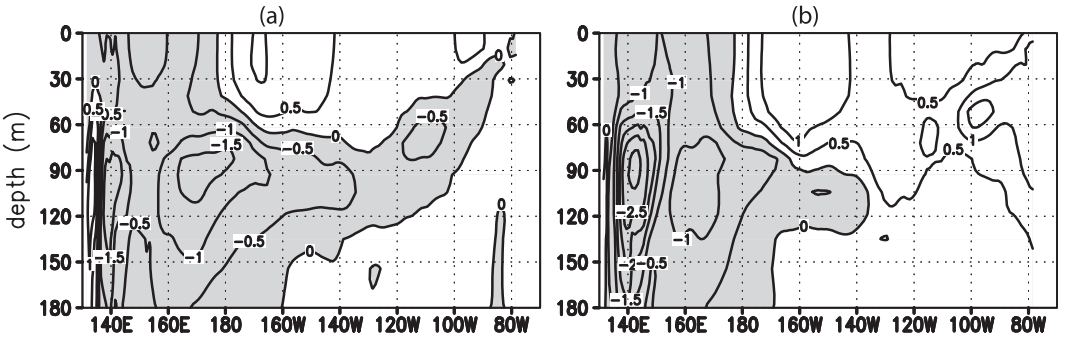

FIG. 11. Vertical cross section at the equator of monthly-mean ocean temperature anomalies (°C) from experiment A in April of year 17 for the (a) anomaly-coupling and (b) normal-coupling ensembles.

again the impact on El Niño events of the seasonal cycle in the eastern basin as described in H1 and not as in H2.

d. Experiment D: Ensembles from 1 October, year 41 of Control (case E41)

Philander (1985), Harrison and Vecchi (1999), and Vecchi and Harrison (2003) hypothesized that the southward shift of convergence zones in the western basin toward the end of the year is responsible for the demise of El Niño events. Uncoupled tests using GCMs also showed evidence supporting this hypothesis (e.g., Spencer 2004; Vecchi and Harrison 2006; Vecchi 2006). Our anomaly-coupling method allows us to examine this hypothesis in a full CGCM. Because we are dealing with a simulated El Niño event rather than with highly idealized anomalies, we can investigate how effective this mechanism is compared to the mechanisms of the ''intrinsic oscillator,'' symbolized by simplified models such as the delayed oscillator. In other words, we can test whether a warm event would still decay at the end of the year without this southward shift and, if not, how significant the difference would be.

Figure 8d shows the evolution of the Niño-3 SSTA indices for all runs in experiment D. The differences between the blue and red lines have substantial magnitudes. For example, by January of year 42, the difference between ensemble averages (thick lines) already exceeds 1°C. The difference in wind stress anomalies in this month is already very telling. As shown in Fig. 15, the westerly anomaly patch for the anomaly-coupling ensemble average is centered on the equator and extends eastward until about 140°W, whereas the westerly anomaly

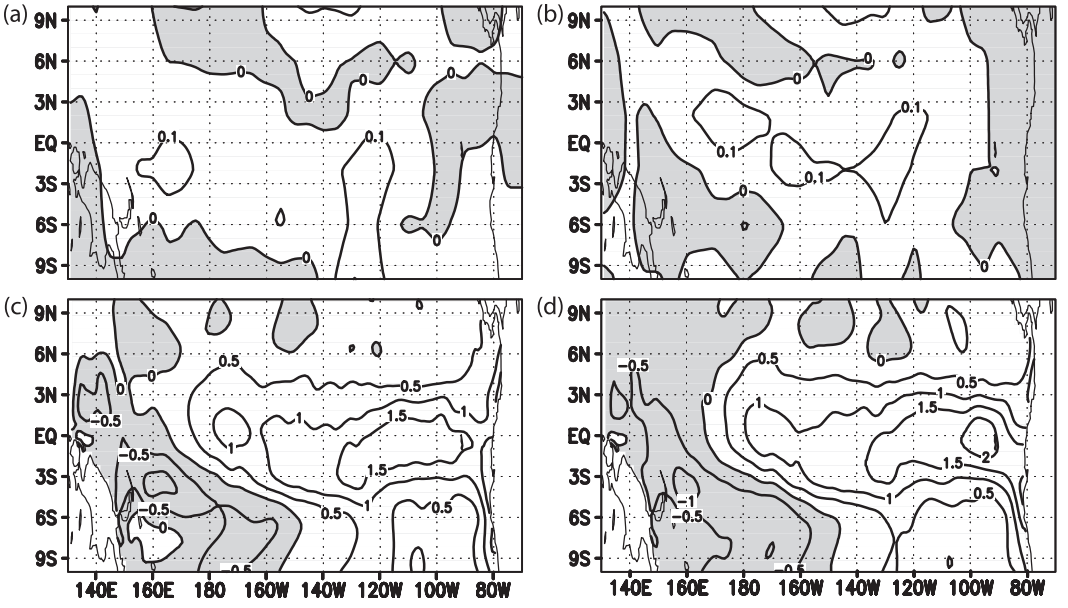

FIG. 12. Monthly mean anomalies from experiment B in June of year 17 of (a),(b) surface zonal wind stress (dyn cm^{-2}) and (c),(d) SST (°C) for (left) the anomaly-coupling and (right) normal-coupling ensembles.

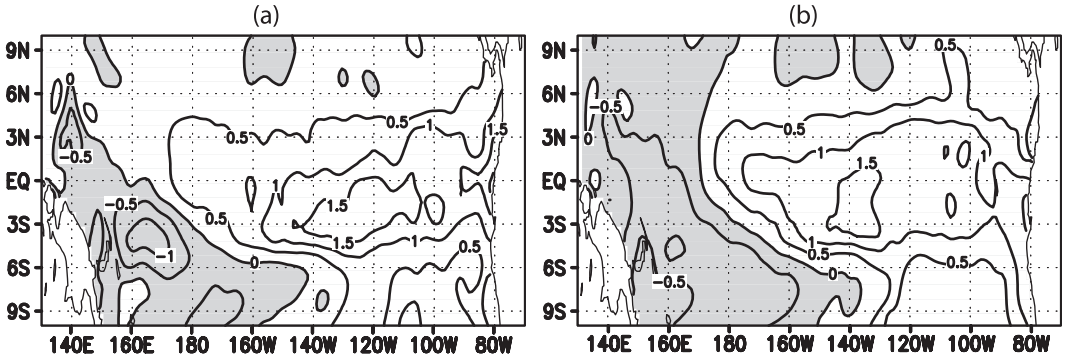

FIG. 13. Monthly mean SST (°C) anomalies from experiment B in July of year 17 for the (a) anomaly-coupling and (b) normal-coupling ensembles.

patch for the normal-coupling ensemble average is strong but shifted south of the equator and stays west of 160°W. In December, this southward shift and the disappearance of the anomalies in the east in the normal-coupling ensemble are already visible in Figs. 16a and 16b. From the temporal evolution of the western to central basin wind stress anomalies in Fig. 17, we can see that in October and November the difference is still small both in terms of strength and spatial structure and that the southward shift begins in December. Accompanying this southward shift, the warm subsurface anomalies start weakening (Figs. 16c,d), the coupled growth in the eastern basin loses strength (wind anomalies disappear in the eastern basin), and the event starts decaying. After January, even the warming of the eastern basin cannot revive the dying event.

Our interpretation of these results is that the seasonal change in the atmosphere from November to January plays an essential role in the decay of the warm event. Furthermore, the growth of warm anomalies in the anomaly-coupling ensemble is not due to more favorable conditions in the east because, compared to the situation in November, the eastern basin actually warms up during that period. The growth is due to the southward movement of the convergence zones in the west. In this regard, the difference between the scenarios proposed by Philander (1985) and Vecchi and Harrison (2003) as to why such a southward migration of the convergence zone in the west basin leads to the decay of the warm event is of secondary importance: the key point in both explanations is the reduction in the equatorial westerly anomalies. It is very likely, however,

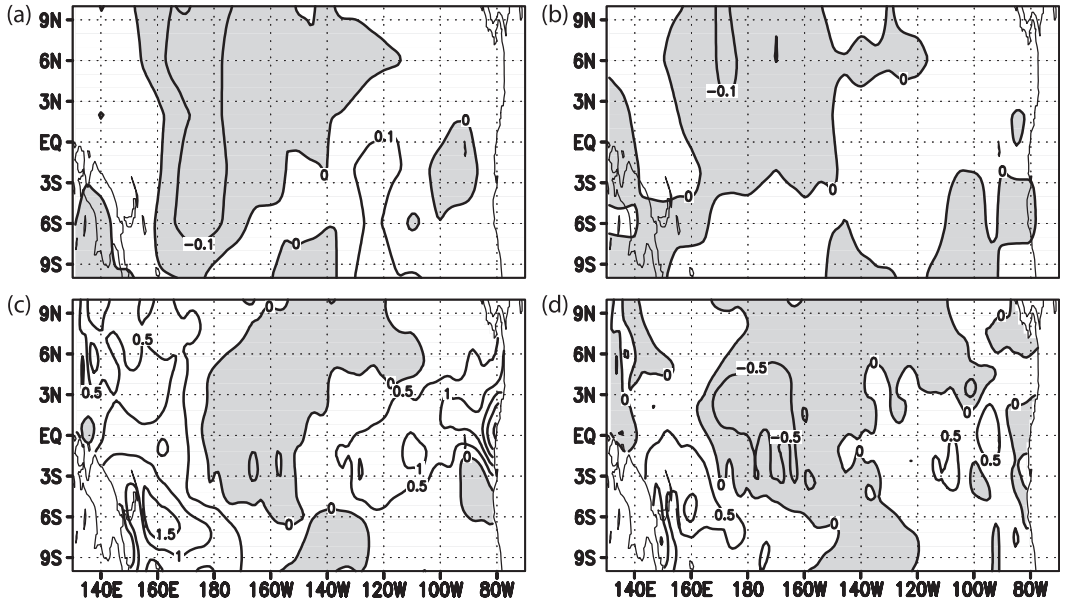

FIG. 14. As in Fig. 12, but for experiment C in July of year 41.

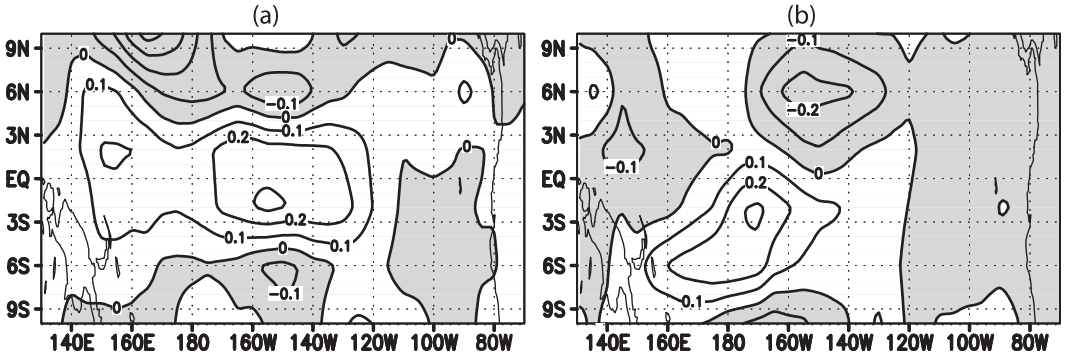

FIG. 15. Monthly mean anomalies from experiment D in January of year 42 of surface zonal wind stress (dyn cm^{-2}) for the (a) anomaly-coupling and (b) normal-coupling ensembles.

that both mechanisms contribute to this reduction, especially if the migration of the convergence zone proceeds smoothly in the November–January period. Thus, the results of experiment D validate H3.

These results are not necessarily inconsistent with the role assigned to oceanic wave signals due to western boundary reflection by classical delayed oscillator theory. Under the delayed oscillator framework, the peaking of an El Niño results from the balance between the warming due to downwelling Kelvin waves generated directly by westerly wind anomalies and the cooling due to upwelling Kelvin waves produced by western boundary

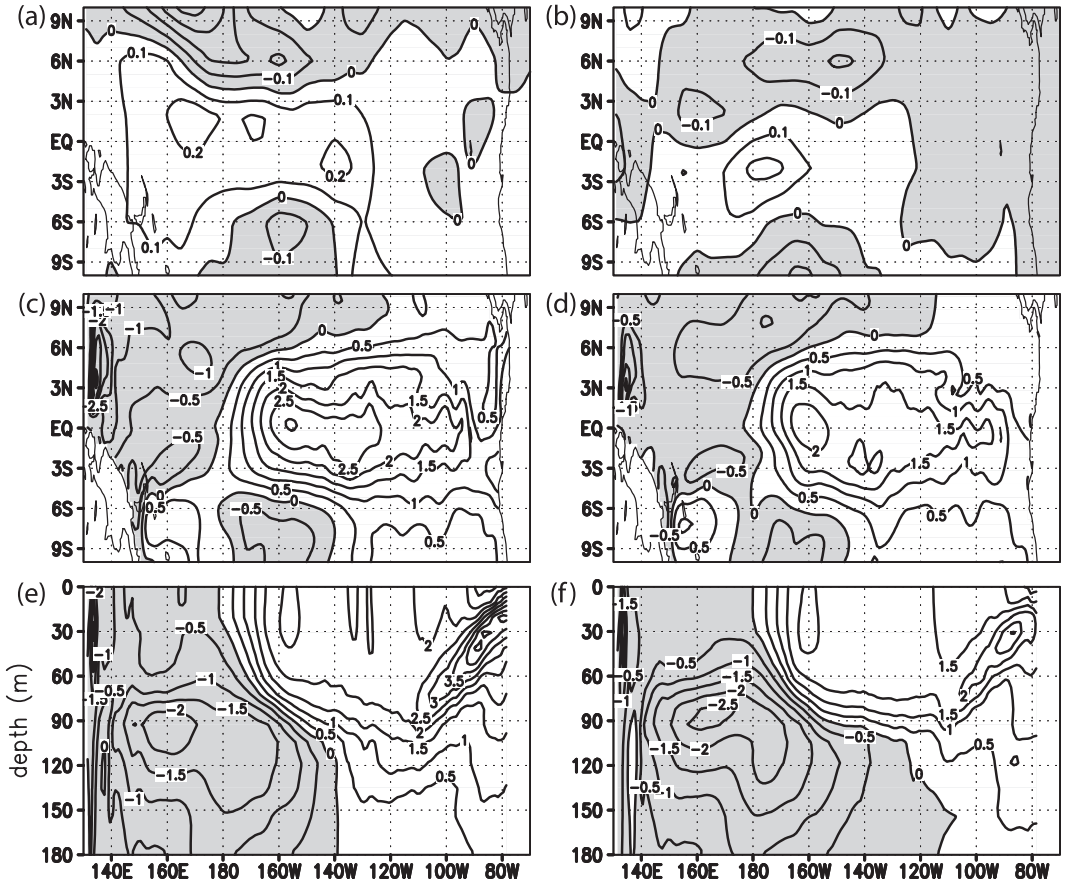

FIG. 16. As in Fig. 12, but for experiment D in December of year 41. (e),(f) Vertical temperature (°C) cross section at the equator for the anomaly-coupling and normal-coupling ensembles, respectively.

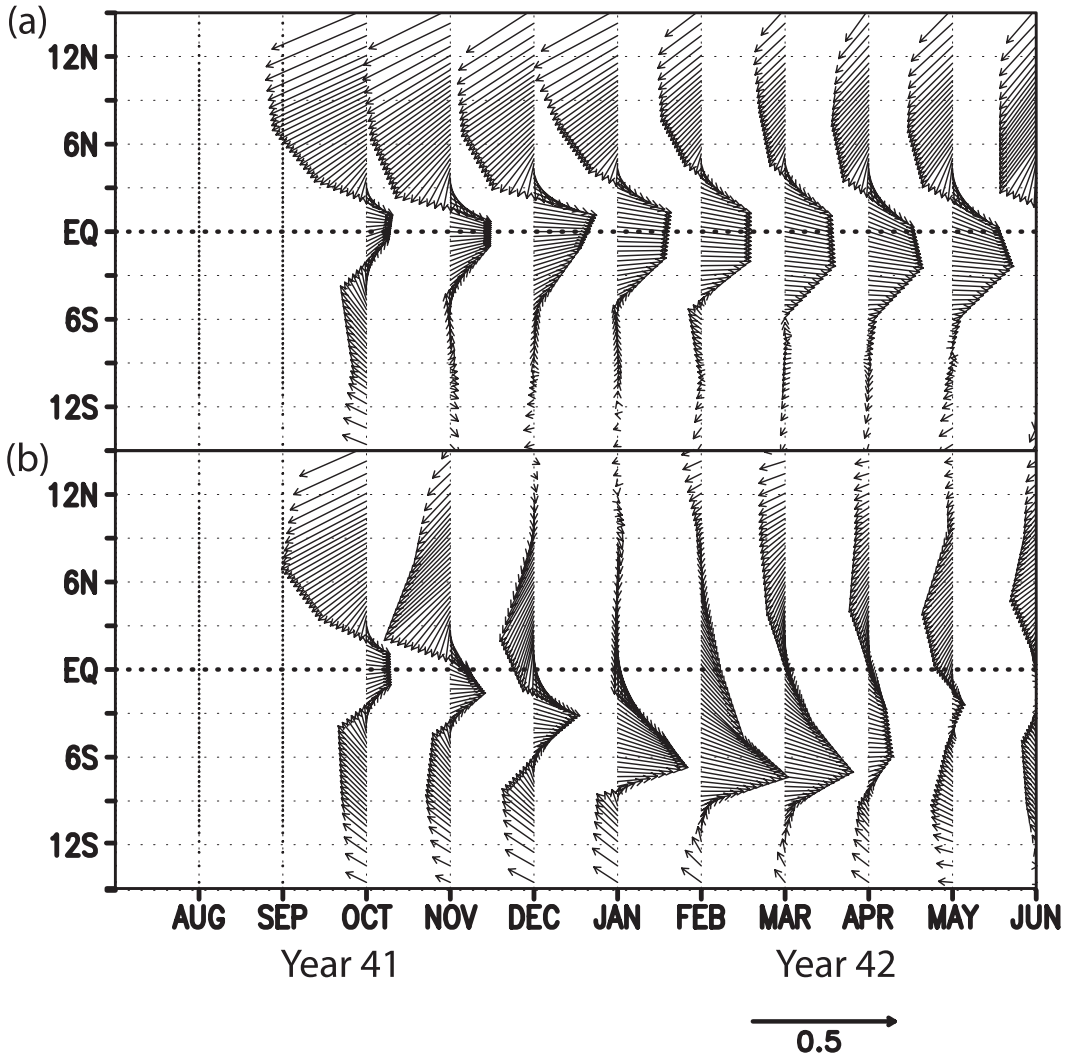

FIG. 17. Evolution of monthly mean surface wind stress anomaly (dyn cm^{-2}; July, year 41–June, year 42) in experiment A averaged in the western to central basin (150°E–170°W) for (a) the anomaly-coupling and (b) normal-coupling ensemble means.

reflection. Our interpretation is that the timing of this balance is modulated by the mean condition and seasonal cycle, the latter of which includes the feature addressed in H3: The seasonal return of surface warm waters to the Southern Hemisphere helps to reduce the warming by shifting the westerly wind anomalies off-equator and thus leads to a balance (peaking) between the warming and cooling signals at the end of the year. When the atmospheric seasonal evolution is artificially frozen and the mean state is fixed to be that of October, a new balance in accordance with this mean state could be achieved later unless this mean condition is unstable. Balance or not, the relevance of delayed oscillator mechanism in the normal-coupling runs cannot be completely denied in our case.

4. Summary

This paper focuses on the validation of the following hypotheses on the relationship between El Niño and the seasonal cycle: H1—The seasonal warming of the cold tongue in the early part of the calendar year (January–April) favors the initial growth of an event; H2—during an event the warm surface waters migrating in the western basin from the Southern to the Northern Hemisphere during the northern spring (April–May) trigger enhanced convection along the equator, which contributes to reinforce the event; and H3—the warm surface waters returning in the western basin from the Northern to the Southern Hemisphere toward the end of the calendar year (November–January) favor the demise of ongoing events.

The method used was based on ensemble simulations with a CGCM of the tropical Pacific. This allows for comparisons of runs with fixed (anomaly coupling) and time-varying (normal coupling) seasonal conditions in the model's atmospheric component only. The work was organized as four experiments (A–D) that targeted specific hypotheses.

From approximately January to April, mean precipitation and convective activity in the eastern equatorial Pacific increases in association with the surface warming of the oceanic cold tongue region. The results we obtain in experiment A show that these seasonal changes reinforce the coupled growth in the central to eastern equatorial basin of low-level winds, SSTs, and oceanic subsurface temperature anomalies. The increase in background convection in the central to eastern equatorial basin favors stronger convective heating and enhanced low-level convergence directly forced by underlying warm SST anomalies. This increase, in general, is associated with stronger westerly wind anomalies slightly to the west (around the date line region), which in turn relate to the increase in the strength of warm surface and subsurface anomalies in the central to eastern basin.

From April to May, the atmospheric convergence zone in the western tropical Pacific migrates from the Southern to the Northern Hemisphere. This migration could trigger an eastward extension of convection along the equator from the western basin (Philander 1985) and increase the westerly wind anomalies in the central basin, thereby amplifying the El Niño event (H2). To validate H2 we considered two warm events, one in which warm SST anomalies are strong throughout April–May and another in which the anomalies are just starting to grow during the same period (experiments B and C, respectively). We find little evidence that the northward migration of the surface warm waters and atmospheric convergence zones in the western basin has a large positive impact on the warm event evolution. The impact of the restrengthening of the cold tongue and the related reduction in coupling instability in the eastern basin, which takes place at the same time of the year, actually dominates in experiment C.

Toward the end of the calendar year (November–January), positive SST anomalies associated with a warm event start decaying in the eastern equatorial basin. Accompanying this decay, westerly wind anomalies around the date line (150°E–170°W) shift southward away from the equator. Our results in experiment D show that SST anomalies in the eastern basin would not decay without such a southward shift in the wind anomaly, which validates H3. In experiment D (as well as in all others) the oceanic seasonal cycle is untouched and the coupling between atmospheric and oceanic anomalies is also intact; the southward shift of the equatorial wind anomalies is prevented by holding back the seasonal southward migration of the atmospheric convergence zones in the mean state. In doing so, the southward migration in equatorial anomalous wind leads to a reduction in the subsurface warm water moving eastward and thus halts the coupled anomalous growth in the central to eastern basin.

In all ensemble simulations we find considerable spreads in the evolution of both SST (Fig. 8) and wind (not shown) anomalies. To assess whether the differences between the two ensembles in our experiments A and D are statistically significant, we apply Student's t tests to Niño-3 SSTA indices and zonal wind stress anomalies averaged in the central to western basin (5°S–5°N, 150°E–170°W). In experiment A, the differences between the Niño-3 SSTA indices of the two ensembles are significant at above the 99% level 2 months after the restart. For the zonal wind stresses averaged in the central to western basin (5°S–5°N, 150°E–170°W), the differences are significant at above the 99% level just 1 month after the restart. In experiment D, the significance levels are even higher.

In summary, the impacts on El Niño events of the atmospheric seasonal change hypothesized by previous studies (Philander 1985; Harrison and Vecchi 1999) do exist, and in some cases are decisive. Because this is necessarily a case study, we conclude that our results verify H1 and H3 in some cases but cannot guarantee that they are valid in all cases; also, they do not wholly invalidate H2 but demonstrate that it is not valid in all cases.

5. Discussion and future work

The UCLA CGCM used in this study produces an interannual oscillation in the tropical Pacific that differs from the observation mainly in two aspects: (i) the magnitude of the model oscillation is weaker and (ii) simulated El Niños tend to peak earlier in the calendar year than the observed ones. We argue, however, that these model difficulties do not raise reasonable challenges to the findings on H1 and H3 summarized in section 4.

First, the simulated seasonal cycle–El Niño phase relation has several realistic features, and to perform our experiments we selected cases with realistic evolutions. For example, the initiation of El Niño events is realistically simulated in the model. As shown in Fig. 4b, the seasonal minimum of Niño-3 SSTA variance around March–April is well captured by the model. This property adds credibility to our conclusions about H1 from experiment A. Also, even though model El Niño events tend to peak early, there are several events (three out of

nine for the 43-yr run), including the one (E41) we chose for the validation of H3, which does peak at the right time of the year.

Second, Neelin et al. (2000; see also our review in the introduction) found, in coupled models of different complexities, high sensitivity of ENSO phase-locking behavior to the basic parameters due to the nonlinearity in the interactions with the seasonal cycle. A slight change in the parameters that control the mean state—which in turn affects the magnitude and period of the intrinsic interannual oscillator, or the strength of the seasonal variation, or the magnitude and phase of the atmospheric high-frequency variability in the model—could lead to significant changes in the apparent ENSO phase-locking behavior. In other words, how statistically significantly the potential of seasonal cycle–ENSO interaction mechanisms are realized is highly sensitive to the setup of the model; under different setups, these mechanisms still work pretty much in the same way for events with similar evolution patterns. This mechanism insensitivity enables us to argue that our CGCM with a reasonable seasonal cycle and interannual variability is appropriate for the kind of mechanistic study we do in this paper. These arguments also support our interpretation of results from experiment D regarding H3.

A close examination of individual simulations in any of the ensembles presented in this paper reveals that the response to differences in the initial conditions can be larger than that to the artificial changes in the seasonal cycle. Furthermore, Xiao and Mechoso (2009) demonstrated that the nonlinear interactions with the seasonal cycle in the upper ocean currents and thermal structure could also be important for ENSO evolution. This was done by selecting ENSO events in a simulation by the same CGCM used in the present study and comparing the evolution of the model's oceanic component with different forcing fields. These fields were obtained by adding the seasonal cycle and the interannual components, both from the CGCM simulation, with different shifts in time. We found that such a time shift can significantly affect the evolution of the heat content anomaly in the equatorial eastern basin. The influence was primarily established through changes in the anomalous zonal advection of temperature in the upper ocean, to which directly forced current anomalies and those caused by delayed effects both contribute. This sensitivity to the oceanic seasonal cycle, together with the sensitivity to initial conditions mentioned above, indicates that the variation in the seasonal cycle phase locking of ENSO in the observation, as well as in CGCM simulations, is ultimately determined by the complex interplay between various interaction mechanisms, the intrinsic ENSO oscillator, and atmospheric high-frequency variability.

Our long-term goal includes a better understanding of the reasons for the deficiencies in the simulated interannual variability compared to observation. As in other CGCMs (Mechoso et al. 1995; de Szoeke and Xie 2008), the simulated mean state in the tropical Pacific has several differences with the observation: the cold tongue is narrower; the thermocline slope along the equator is different, especially in the central basin, where it is flatter; and the SST field has a general warm bias, especially in the eastern basin. Such differences may contribute to the overall weaker interannual oscillation in the simulation. Therefore, we are working on the reduction and eventual elimination of CGCM systematic errors by improving parameterizations of physical processes in the model (e.g., Konor and Arakawa 2008). Also, the CGCM produces considerably weaker high-frequency variability in the tropical atmosphere compared to observation. According to several studies (McPhaden et al. 2006; Chang et al. 2007; Hendon et al. 2007), springtime westerlies associated with high-frequency atmospheric variability in the central to western basin can lead to more intensive development of El Niño events later in the year. The lack of such springtime high-frequency variability in the model may cause model El Niño events to be weaker and peak prematurely in comparison to the observed ones. In this context, we are considering artificial enhancement to the simulated high-frequency variability.

Acknowledgments. This research was supported by NOAA Grants NA03OAR4310095 and NA07OAR4310236.

REFERENCES

Alexander, R. C., and R. L. Mobley, 1976: Monthly average sea-surface temperatures and ice-pack limits on a 1° global grid. *Mon. Wea. Rev.,* **104,** 143–148.

An, S.-I., and B. Wang, 2001: Mechanisms of locking of the El Niño and La Niña mature phases to boreal winter. *J. Climate,* **14,** 2164–2176.

Arakawa, A., and W. H. Schubert, 1974: Interaction of a cumulus cloud ensemble with the large-scale environment, Part I. *J. Atmos. Sci.,* **31,** 674–701.

Battisti, D. S., and A. C. Hirst, 1989: Interannual variability in the tropical atmosphere–ocean system: Influence of the basic state and ocean geometry. *J. Atmos. Sci.,* **46,** 1687–1712.

Bryan, K., 1969: A numerical method for the study of the circulation of the world ocean. *J. Comput. Phys.,* **4,** 347–376.

Burgers, G., and D. B. Stephenson, 1999: The ''normality'' of El Niño. *Geophys. Res. Lett.,* **26,** 1027–1030.

Chang, P., L. Zhang, R. Saravanan, D. J. Vimont, J. C. H. Chiang, L. Ji, H. Seidel, and M. K. Tippett, 2007: Pacific meridional mode and El Niño–Southern Oscillation. *Geophys. Res. Lett.,* **34,** L16608, doi:10.1029/2007GL030302.

Cox, M. D., 1984: A primitive equation three-dimensional model of the ocean. GFDL Ocean Group Tech. Rep. 1, 75 pp.

Deardorff, J. W., 1972: Parameterization of the planetary boundary layer for use in general circulation models. *Mon. Wea. Rev.,* **100,** 93–106.

de Szoeke, S. P., and S.-P. Xie, 2008: The tropical eastern Pacific seasonal cycle: Assessment of errors and mechanisms in IPCC AR4 coupled ocean–atmosphere general circulation models. *J. Climate,* **21,** 2573–2590.

Eisenman, I., L. S. Yu, and E. Tziperman, 2005: Westerly wind bursts: ENSO's tail rather than the dog? *J. Climate,* **18,** 5224–5238.

Galanti, E., E. Tziperman, M. Harrison, A. Rosati, R. Giering, and Z. Sirkes, 2002: The equatorial thermocline outcropping—A seasonal control on the tropical Pacific ocean–atmosphere instability strength. *J. Climate,* **15,** 2721–2739.

Graham, N. E., and T. P. Barnett, 1987: Sea surface temperature, surface wind divergence, and convection over tropical oceans. *Science,* **238,** 657–659.

Guilyardi, E., P. Delecluse, S. Gualdi, and A. Navarra, 2003: Mechanisms of ENSO phase change in a coupled GCM. *J. Climate,* **16,** 1141–1158.

Harrison, D. E., and G. A. Vecchi, 1999: On the termination of El Niño. *Geophys. Res. Lett.,* **26,** 1593–1596.

Harshvardhan, R. Davis, D. A. Randall, and T. G. Corsetti, 1987: A fast radiation parameterization for general circulation models. *J. Geophys. Res.,* **92,** 1009–1016.

Hendon, H. H., M. C. Wheeler, and C. Zhang, 2007: Seasonal dependence of the MJO–ENSO relationship. *J. Climate,* **20,** 531–543.

Jiang, N., J. D. Neelin, and M. Ghil, 1995: Quasi-quadrennial and quasi-biennial variability in the equatorial Pacific. *Climate Dyn.,* **12,** 101–112.

Katayama, A., 1972: A simplified scheme for computing radiative transfer in the troposphere. Numerical Simulation of Weather and Climate Tech. Rep. 6, 77 pp.

Kessler, W. S., 2002: Is ENSO a cycle or a series of events? *Geophys. Res. Lett.,* **29,** 2125, doi:10.1029/2002GL015924.

——, and R. Kleeman, 2000: Rectification of the Madden–Julian oscillation into the ENSO cycle. *J. Climate,* **13,** 3560–3575.

Kim, Y.-J., and A. Arakawa, 1995: Improvement of orographic gravity wave parameterization using a mesoscale gravity wave model. *J. Atmos. Sci.,* **52,** 1875–1902.

Kirtman, B. P., J. Shukla, B. Huang, Z. Zhu, and E. K. Schneider, 1997: Multiseasonal predictions with a coupled tropical ocean–global atmosphere system. *Mon. Wea. Rev.,* **125,** 789–808.

Konor, C. S., and A. Arakawa, cited 2008: Incorporation of a PBL parameterization into a general circulation model. [Available online at http://kiwi.atmos.colostate.edu/pubs/New_PBL_Tech_Rep_sigma_GCM.pdf.]

Li, J.-L., C. R. Mechoso, and A. Arakawa, 1999: Improved PBL moist processes with the UCLA GCM. Preprints, *Ninth Conf. on Climate Change,* Dallas, TX, Amer. Meteor. Soc., 423–426.

Locarnini, R. A., A. V. Mishonov, J. I. Antonov, T. P. Boyer, and H. E. Garcia, 2006: *Temperature*. Vol. 4, *World Ocean Atlas 2005,* NOAA Atlas NESDIS 61, 182 pp.

McPhaden, M. J., 1999: Genesis and evolution of the 1997–98 El Niño. *Science,* **283,** 950–954.

——, F. Bahr, Y. DuPenhoat, E. Firing, S. P. Hayes, P. P. Niiler, P. L. Richardson, and J. M. Toole, 1992: The response of the western equatorial Pacific Ocean to westerly wind bursts during November 1989 to January 1990. *J. Geophys. Res.,* **97,** 14 289–14 303.

——, X. Zhang, H. H. Hendon, and M. C. Wheeler, 2006: Large scale dynamics and MJO forcing of ENSO variability. *Geophys. Res. Lett.,* **33,** L16702, doi:10.1029/2006GL026786.

Mechoso, C. R., and Coauthors, 1995: The seasonal cycle over the tropical Pacific in coupled ocean–atmosphere general circulation models. *Mon. Wea. Rev.,* **123,** 2825–2838.

——, J.-Y. Yu, and A. Arakawa, 2000: A coupled GCM pilgrimage: From climate catastrophe to ENSO simulations. *General Circulation Model Development: Past, Present, and Future,* D. A. Randall, Ed., Academic Press, 539–575.

——, J. D. Neelin, and J.-Y. Yu, 2003: Testing simple models of ENSO. *J. Climate,* **60,** 305–318.

Mellor, G. L., and T. Yamada, 1982: Development of a turbulence closure model for geophysical fluid problems. *Rev. Geophys.,* **20,** 851–875.

Moore, A. M., and R. Kleeman, 1999: Stochastic forcing of ENSO by the intraseasonal oscillation. *J. Climate,* **12,** 1199–1220.

Neelin, J. D., D. S. Battisti, A. C. Hirst, F.-F. Jin, Y. Wakata, T. Yamagata, and S. Zebiak, 1998: ENSO theory. *J. Geophys. Res.,* **103,** 14 261–14 290.

——, F.-F. Jin, and H.-H. Syu, 2000: Variations in ENSO phase locking. *J. Climate,* **13,** 2570–2590.

Pacanowski, R. C., K. W. Dixon, and A. Rosati, 1991: The GFDL Modular Ocean Model user guide. GFDL Ocean Group Tech. Rep. 2, 75 pp.

Philander, S. G. H., 1985: El Niño and La Niña. *J. Atmos. Sci.,* **42,** 2652–2662.

——, T. Yamagata, and R. Pacanowski, 1984: Unstable air–sea interactions in the tropics. *J. Atmos. Sci.,* **41,** 604–613.

Roulston, M. S., and J. D. Neelin, 2000: The response of an ENSO model to climate noise, weather noise and intraseasonal forcing. *Geophys. Res. Lett.,* **27,** 3723–3726.

Smith, T. M., R. W. Reynolds, T. C. Peterson, and J. Lawrimore, 2007: Improvements to NOAA's historical merged land–ocean surface temperature analysis (1880–2006). *J. Climate,* **21,** 2283–2296.

Spencer, H., 2004: Role of the atmosphere in seasonal phase locking of El Niño. *Geophys. Res. Lett.,* **31,** L24104, doi:10.1029/2004GL021619.

Suarez, M. J., A. Arakawa, and D. A. Randall, 1983: The parameterization of the planetary boundary layer in the UCLA general circulation model: Formulation and results. *Mon. Wea. Rev.,* **111,** 2224–2243.

Torrence, C., and G. P. Compo, 1998: A practical guide to wavelet analysis. *Bull. Amer. Meteor. Soc.,* **79,** 61–78.

Tziperman, E., L. Stone, M. A. Cane, and H. Jarosh, 1994: El Niño chaos: Overlapping of resonances between the seasonal cycle and the Pacific Ocean–atmosphere oscillator. *Science,* **264,** 72–74.

——, M. A. Cane, and S. E. Zebiak, 1995: Irregularity and locking to the seasonal cycle in an ENSO prediction model as explained by the quasi-periodicity route to chaos. *J. Atmos. Sci.,* **52,** 293–306.

——, S. E. Zebiak, and M. A. Cane, 1997: Mechanisms of seasonal–ENSO interaction. *J. Atmos. Sci.,* **54,** 61–71.

——, M. A. Cane, S. E. Zebiak, Y. Xue, and B. Blumenthal, 1998: Locking of El Niño's peak time to the end of the calendar year in the delayed oscillator picture of ENSO. *J. Climate,* **11,** 2191–2199.

Vecchi, G. A., 2006: The termination of the 1997–98 El Niño. Part II: Mechanisms of atmospheric change. *J. Climate,* **19,** 2647–2664.

——, and D. E. Harrison, 2000: Tropical Pacific sea surface temperature anomalies, El Niño, and equatorial westerly wind events. *J. Climate,* **13,** 1814–1830.

——, and ——, 2003: On the termination of the 2002–2003 El Niño event. *Geophys. Res. Lett.,* **30,** 1964, doi:10.1029/2003GL017564.

——, and ——, 2006: The termination of the 1997–98 El Niño. Part I: Mechanisms of oceanic change. *J. Climate,* **19,** 2633–2646.

Vintzileos, A., P. Delecluse, and R. Sadourny, 1999: On the mechanisms in a tropical ocean–global atmosphere coupled general circulation model. Part II: Interannual variability and its relation to the seasonal cycle. *Climate Dyn.,* **15,** 63–80.

Wang, B., R. Wu, and R. Lukas, 1999: Roles of the western North Pacific wind variation in thermocline adjustment and ENSO phase transition. *J. Meteor. Soc. Japan,* **77,** 1–16.

Xiao, H., 2008: A GCM study of ENSO and its relationship with the seasonal cycle. Ph.D. dissertation, Department of Atmospheric and Oceanic Sciences, University of California, Los Angeles, 187 pp.

——, and C. R. Mechoso, 2009: Correlative evolutions of ENSO and the seasonal cycle in the tropical Pacific Ocean. *J. Atmos. Sci.,* **66,** 1041–1049.

Xie, P., and P. A. Arkin, 1997: Global precipitation: A 17-year monthly analysis based on gauge observations, satellite estimates, and numerical model outputs. *Bull. Amer. Meteor. Soc.,* **78,** 2539–2558.

Yu, J.-Y., and C. R. Mechoso, 2001: A coupled atmosphere–ocean GCM study of the ENSO cycle. *J. Climate,* **14,** 2329–2350.

Zebiak, S. E., and M. A. Cane, 1987: A model El Niño–Southern Oscillation. *Mon. Wea. Rev.,* **115,** 2262–2278.